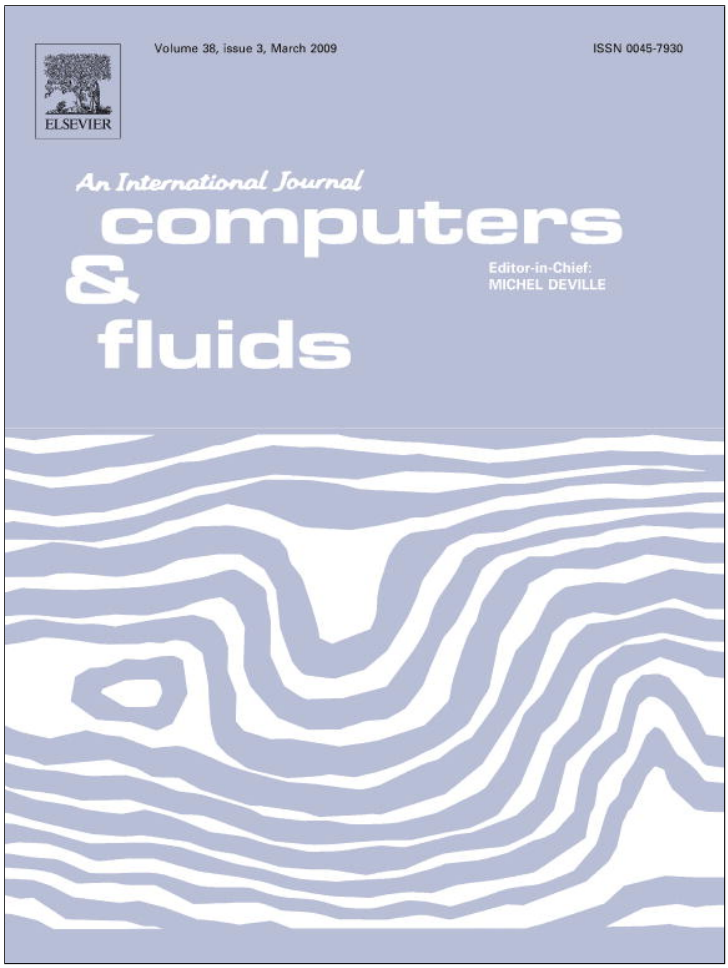

Computers & Fluids 38 (2009) 564–571

Contents lists available at ScienceDirect

Computers & Fluids

journal homepage: www.elsevier.com/locate/compfluid

Numerical simulation of particle encapsulation due to liquid thread breakup

Haoxiang Luo [a,*], C. Pozrikidis [b]

[a] Department of Mechanical Engineering, Vanderbilt University, 2301 Vanderbilt Pl., Nashville, TN 37235-1592, USA
[b] Department of Mechanical and Aerospace Engineering, University of California, San Diego, La Jolla, CA 92093-0411, USA

ARTICLE INFO

Article history:
Received 14 January 2008
Received in revised form 28 April 2008
Accepted 25 May 2008
Available online 4 June 2008

ABSTRACT

The capillary instability of a liquid thread containing a periodic array of particles along the centerline is considered with reference to micro-encapsulation. The Navier–Stokes equation for axisymmetric flow inside and outside the thread is solved using an immersed boundary method implemented on a boundary-fitted orthogonal curvilinear grid that conforms with the particle shape. Numerical simulations are carried out to investigate the effect of the particle spacing, viscosity ratio, Reynolds number, and waveform of interfacial perturbations. The results show that fluid inertia delays the onset of the instability and may have an important effect on the number and volume of developing pure and encapsulating drops. The effect of the particle size diminishes as the Reynolds number is raised. An insoluble surfactant significantly delays the interfacial amplification and affects the process of thread breakup and the details of particle encapsulation.

1. Introduction

A liquid suspension of small particles ejected through a micronozzle to form a thread disintegrates into small droplets due to the Rayleigh capillary instability (e.g. [1]). Some droplets contain pure liquid, other droplets encapsulate particles inside annular shells. Micro-encapsulation techniques based on thread breakup are of considerable interest in the food, biomedical, and pharmaceutical industry where small particles, cells, and cell agglomerates are produced and dispersed in an ambient medium. Encapsulation efficiency is of primary importance in the biomedical industry, as reviewed by Orive et al. [2].

The capillary instability and ultimate disintegration of pure liquid threads, jets, and annular layers have received a great deal of attention in the fundamental and applied literature (e.g. [3–6]). A few laboratory studies have addressed the encapsulation of bubbles and cells [1,7–9]. Blyth and Pozrikidis [10] recently carried out a normal mode linear stability analysis of a thread hosting a regular array of spherical particles deployed along the centerline, under conditions of Stokes flow. The results revealed that, at small particle separations, the interfacial profiles are nearly sinusoidal waves whose growth rate is nearly equal to that of the pure thread. Harmonic constituents suddenly enter the normal modes for moderate and large particle separations, elevating the growth rates and yielding a stability diagram that consists of a sequence of superposed pure thread lobes. A complementary numerical stability analysis based on the boundary-integral formulation for Stokes flow for fluids with equal viscosity revealed that particles whose radius is comparable to the thread radius have a strong stabilizing influence. Blyth and Pozrikidis [10] also performed boundary-integral method for Stokes flow and demonstrated that thread breakup leads to particles coated with annular layers of different thickness.

In this work, the onset and progress of the capillary instability is investigated at nonzero Reynolds numbers beyond the confines of linear stability analysis, and the effect of the fluid viscosities, fluid inertia, particle size and spacing, insoluble surfactant, and form of the interfacial perturbation is considered. The investigation relies on numerical solutions of the Navier–Stokes equation using Peskin's immersed-interface formulation (e.g. [11]), combined with a finite-difference method implemented on an orthogonal curvilinear grid constructed by conformal mapping. A similar method was implemented by Blyth et al. [12] for computing the evolution of axisymmetric waves in core-annular flow on a rectilinear grid, and by Luo et al. [13] for computing two-layer flow in a corrugated channel on an orthogonal grid. The results will reveal that fluid inertia may have a significant effect on the onset and progress of the instability.

2. Problem formulation and governing equations

We consider the instability of a cylindrical thread of a liquid with radius b and viscosity μ_1 suspended in an effectively infinite ambient fluid with viscosity μ_2, as shown in Fig. 1. An array of evenly spaced spherical particles with radius $a < b$ is deployed along the centerline. The densities of the two fluids are matched, and the particles are neutrally buoyant. The interface between the thread and the ambient fluid is occupied by an insoluble surfactant. The Rayleigh capillary instability due to the interfacial tension causes the cylindrical thread surface to develop periodic

* Corresponding author. Tel.: +1 615 322 2079.
E-mail address: haoxiang.luo@vanderbilt.edu (H. Luo).

0045-7930/$ - see front matter © 2008 Elsevier Ltd. All rights reserved.
doi:10.1016/j.compfluid.2008.05.004

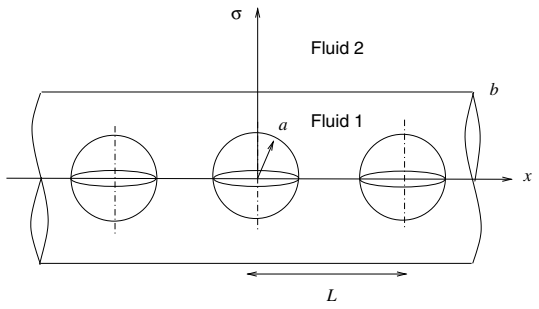

Fig. 1. A liquid thread hosting an array of spherical particles along the centerline.

corrugations of increasing amplitude and eventually disintegrate into an array of drops encapsulating the particles. We consider the instability subject to periodic axisymmetric perturbations whose wavelength is equal to the particle spacing, L, and describe the motion in cylindrical polar coordinates (x,σ), where σ is the distance from the x-axis.

The flow in each fluid is governed by the Navier–Stokes equation and the continuity equation for incompressible fluids

$$\rho\left(\frac{\partial \mathbf{u}}{\partial t}+\mathbf{u}\cdot\nabla\mathbf{u}\right)=-\nabla p+\mu_j\nabla^2\mathbf{u},\quad \nabla\cdot\mathbf{u}=0, \tag{1}$$

where $\mathbf{u}$ is the velocity, p is the hydrodynamic pressure incorporating hydrostatic variations, ρ are is the densities, μ_j are the viscosities, and $j=1$, 2 correspond to the thread and ambient fluid, respectively. The velocity satisfies the no-slip and no-penetration conditions at the particle surface and varies continuously across the interface. A periodicity condition is imposed along the thread axis. The hydrodynamic traction undergoes a discontinuity across the interface, given by

$$(\boldsymbol{\tau}^{(1)}-\boldsymbol{\tau}^{(2)})\cdot\mathbf{n}=\gamma 2\kappa_m\mathbf{n}-\frac{\partial\gamma}{\partial l}\mathbf{t}, \tag{2}$$

where $\boldsymbol{\tau}^{(j)}$ is the Newtonian stress tensor in the jth fluid evaluated on either side of the interface, γ is the surface tension, $\mathbf{n}$ is the unit normal vector pointing into the thread, $\mathbf{t}$ is the unit tangent vector along the contour of the interface in a meridional plane pointing in the direction of increasing arc length l, and $\kappa_m\equiv\frac{1}{2}\nabla\cdot\mathbf{n}$ is the mean curvature. The last term on the right-hand side of (2) is the Marangoni traction due to variations in the surface tension associated with the presence of an insoluble surfactant.

The surface concentration of the surfactant, Γ, is governed by the convection–diffusion equation

$$\frac{\mathrm{d}\Gamma}{\mathrm{d}t}=w\frac{\partial\Gamma}{\partial l}-\frac{1}{\sigma}\frac{\partial(\sigma u_t\Gamma)}{\partial l}-2\kappa_m u_n\Gamma+\frac{D_s}{\sigma}\frac{\partial}{\partial l}\left(\sigma\frac{\partial\Gamma}{\partial l}\right), \tag{3}$$

where $u_t=\mathbf{u}\cdot\mathbf{t}$ and $u_n=\mathbf{u}\cdot\mathbf{n}$ are the tangential and normal interfacial velocities (e.g. [14,15]). In practice, the surfactant diffusivity, D_s, is very small, and the diffusion term in (3) makes a negligible contribution. The derivative d/dt on the left-hand side of (3) expresses the rate of change of a variable following the motion of an interfacial marker point moving normal to the interface and with an arbitrary tangential velocity, $w(l)$. If $w=u_t$, the marker points are Lagrangian point particles moving with the fluid velocity.

When the surfactant concentration is well below the saturation level, a linear relationship can be assumed between the surface tension and the surfactant concentration according to Gibbs' law, $\gamma_c-\gamma=\Gamma E$, where E is the surface elasticity and γ_c is the surface tension of a clean interface devoid of surfactants (e.g. [16,17]). In terms of the dimensionless physiochemical parameter $\beta=\Gamma_0 E/\gamma_c$, the linear equation of state reads

$$\gamma=\frac{\gamma_0}{1-\beta}\left(1-\beta\frac{\Gamma}{\Gamma_0}\right), \tag{4}$$

where Γ_0 is a reference concentration corresponding to the surface tension $\gamma_0=\gamma_c(1-\beta)$. The significance of the surfactant is expressed by the dimensionless Marangoni number, $Ma=E\Gamma_0/\gamma_0=\beta/(1-\beta)$.

The flow configuration is determined by the fundamental wave number scaled by the inverse of the thread radius, $kb=2\pi b/L$, ratio of the particle size to the thread radius, a/b, viscosity ratio, $\lambda\equiv\mu_2/\mu_1$, Marangoni number, Ma, and Reynolds number $Re=\rho\gamma_0 b/\mu_1^2$. Our objective is to compute the evolution of the interface from a given initial condition, and thus describe the onset, progress, and long term consequences of the instability.

Blyth and Pozrikidis [10] performed a normal mode linear stability analysis in the limit of Stokes flow, $Re=0$. In their formulation, the interfacial shape is expressed as a Fourier series whose fundamental wave number corresponds to the particle spacing,

$$\sigma=b+\epsilon b\mathrm{e}^{st}\sum_{m=1}^{\infty}A_m\cos(mkx), \tag{5}$$

where ϵ is a small dimensionless parameter, A_m are unknown Fourier coefficients, and s is the complex grow rate. The stream function is decomposed into a regular component described by a Fourier series, and a singular component associated with rotational and irrotational singularities of axisymmetric Stokes flow placed inside the particles. Eqs. (2) and (3) are linearized, and an eigenvalue problem is formulated for s whose eigenvectors are Fourier coefficients describing normal modes.

Fig. 2 shows graphs of the reduced growth rate, $S=Re(s)(b\mu_1)/\gamma_0$, of the two most dangerous modes for $a/b=0.2$, $\lambda=0.5$, and $Ma=0.0$. As kb decreases from the Rayleigh threshold of unity, the dominant loaded-thread modes lock on to the fundamental pure thread mode and its first harmonic. The growth rate of the

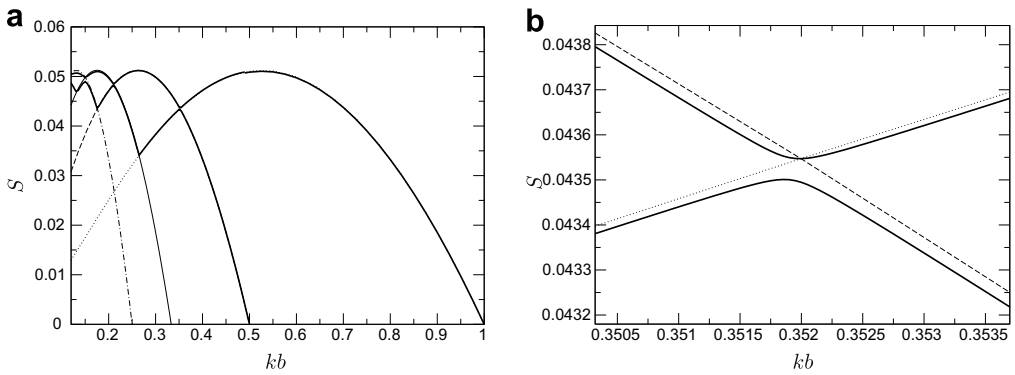

Fig. 2. (a) Linear growth rates of the two dominant modes for $Re=0$, $a/b=0.2$, $\lambda=0.5$, and $Ma=0.0$; (b) close-up of (a). The growth rate of a pure thread and its first three harmonics are shown as thin dotted, thin broken, thin solid, and thin dot-dashed lines, respectively.

fundamental pure thread mode coincides with the growth rate of its first harmonic at $k = 0.352$. At this crossover point, the dominant loaded-thread mode jumps from the fundamental pure thread mode to its first harmonic. Simultaneously, the second most dangerous loaded-thread mode jumps from the first harmonic to the fundamental mode. The interchange is shown in close-up in Fig. 2b. As kb is further reduced, similar behavior takes place at the crossover points of the higher harmonics of the pure thread mode, indicated by the multiple peaks of the two loaded-thread modes. Physically, the particles allow all superharmonics of the fundamental wave number determined by the particle spacing to enter the normal modes, and thereby permit the most unstable available harmonic wave of the pure thread to dominate the motion.

3. Numerical method

To solve the Navier–Stokes equation, we introduce a boundary-fitted orthogonal grid that conforms with the particle array. The grid is generated by conformally mapping one period of the flow in a meridional plane to a rectangular region in the parametric $\xi\eta$ plane, $0 \leqslant \xi \leqslant L$, $0 \leqslant \eta \leqslant \eta_t$, where η_t is a chosen truncation level, as shown in Fig. 3. The mapping is mediated by the function

$$(x, \sigma) = \mathscr{F}(\xi, \eta). \tag{6}$$

The inverse mapping function is

$$\xi = x + \frac{2\alpha}{k}\frac{\sin kx}{\cosh k\sigma - \cos kx}, \quad \eta = \sigma - \frac{2\alpha}{k}\frac{\sinh k\sigma}{\cosh k\sigma - \cos kx}, \tag{7}$$

where $\alpha = (1 - \cos ka)/2$ is a dimensionless coefficient and a is the particle radius [18]. The particle end-point $(a, 0)$ is mapped to the point $(\xi_s, 0)$, where $\xi_s = a + \sin(ka)/k$. The Jacobian of the transformation is

$$\mathbf{J} \equiv \begin{bmatrix} \cos\theta & -\sin\theta \\ \sin\theta & \cos\theta \end{bmatrix} = \frac{1}{\mathscr{J}}\begin{bmatrix} \frac{\partial x}{\partial \xi} & \frac{\partial x}{\partial \eta} \\ \frac{\partial \sigma}{\partial \xi} & \frac{\partial \sigma}{\partial \eta} \end{bmatrix}, \quad \mathscr{J} \equiv \sqrt{\left(\frac{\partial x}{\partial \xi}\right)^2 + \left(\frac{\partial x}{\partial \eta}\right)^2}, \tag{8}$$

where θ is the local clockwise rotation angle at the intersection of the curvilinear and Cartesian coordinates. In practice, the grid is generated by solving nonlinear equation (7) using Newton's method.

The velocity field in a meridional plane is described in terms of its curvilinear components, u_ξ and u_η. The generalized Navier–Stokes equation in the $\xi\eta$ plane incorporating the jump in viscosity and traction across the interface takes the form

$$\rho\left(\frac{\partial \hat{\mathbf{u}}}{\partial t} + \hat{\mathbf{v}}\cdot\hat{\nabla}\hat{\mathbf{u}}\right) = -\hat{\nabla}p + \mu\hat{\nabla}^2\hat{\mathbf{u}} + \hat{\nabla}\mu\times\hat{\omega} + \hat{\mathbf{B}}, \tag{9}$$

where $\hat{u} = (u_\xi, u_\eta)$, $\hat{\mathbf{v}} \equiv \hat{\mathbf{u}} - (2/\rho)\hat{\nabla}\mu$ is a modified velocity, $\hat{\omega} \equiv \hat{\nabla}\times\hat{\mathbf{u}}$ is the vorticity vector in the $\xi\eta$ plane, $\hat{\mathbf{B}}$ is the body force vector accounting for the jump in the interfacial traction

$$\hat{\mathbf{B}}(\boldsymbol{\xi}) = \hat{\mathbf{B}}(\mathscr{F}^{-1}(\mathbf{x})) = -\mathbf{J}^{-1}(\mathbf{x})\cdot\int_I \mathscr{D}_2(\mathbf{x}-\mathbf{x}')\Delta\mathbf{f}(\mathbf{x}')\mathrm{d}l(\mathbf{x}'), \tag{10}$$

$\mathscr{F}^{-1}(\mathbf{x})$ is the inverse mapping from the xy to the $\xi\eta$ plane, and $\Delta\mathbf{f}$ is defined in (2) (e.g. [13]). A caret denotes that the underlying vector or operator is expressed in the working curvilinear coordinates. The expressions for $\hat{\nabla}\hat{\mathbf{u}}$ and $\hat{\nabla}^2\hat{\mathbf{u}}$ are

$$\hat{\nabla}\hat{\mathbf{u}} = \begin{bmatrix} \frac{1}{\mathscr{J}}\frac{\partial u_\xi}{\partial \xi} + \frac{u_\eta}{\mathscr{J}^2}\frac{\partial \mathscr{J}}{\partial \eta} & \frac{1}{\mathscr{J}}\frac{\partial u_\xi}{\partial \eta} - \frac{u_\eta}{\mathscr{J}^2}\frac{\partial \mathscr{J}}{\partial \xi} \\ \frac{1}{\mathscr{J}}\frac{\partial u_\eta}{\partial \xi} - \frac{u_\xi}{\mathscr{J}^2}\frac{\partial \mathscr{J}}{\partial \eta} & \frac{1}{\mathscr{J}}\frac{\partial u_\eta}{\partial \eta} + \frac{u_\xi}{\mathscr{J}^2}\frac{\partial \mathscr{J}}{\partial \xi} \end{bmatrix} \tag{11}$$

and

$$\hat{\nabla}^2\hat{\mathbf{u}} = \frac{1}{\mathscr{J}^2}\begin{bmatrix} \frac{\partial}{\partial\xi}\left(\frac{1}{\sigma}\frac{\partial \sigma u_\xi}{\partial \xi}\right) + \frac{1}{\sigma}\frac{\partial}{\partial\eta}\left(\sigma\frac{\partial u_\xi}{\partial \eta}\right) + c_1u_\xi + c_2u_\eta + c_3\frac{u_\eta}{\partial\xi} + c_4\frac{u_\eta}{\partial\eta} \\ \frac{1}{\sigma}\frac{\partial}{\partial\xi}\left(\sigma\frac{\partial u_\eta}{\partial \xi}\right) + \frac{\partial}{\partial\eta}\left(\frac{1}{\sigma}\frac{\partial \sigma u_\eta}{\partial \eta}\right) + d_1u_\eta + d_2u_\xi + d_3\frac{u_\xi}{\partial\xi} + d_4\frac{u_\xi}{\partial\eta} \end{bmatrix}, \tag{12}$$

where

$$\begin{aligned} c_1 &\equiv -\left[\frac{1}{\mathscr{J}}\left(\frac{\partial^2\mathscr{J}}{\partial\xi^2} + \frac{\partial^2\mathscr{J}}{\partial\eta^2}\right) + \frac{2}{\sigma}\frac{\partial^2\sigma}{\partial\xi^2} + \frac{1}{\mathscr{J}\sigma}\left(\frac{\partial\sigma}{\partial\eta}\frac{\partial\mathscr{J}}{\partial\eta} - \frac{\partial\sigma}{\partial\xi}\frac{\partial\mathscr{J}}{\partial\xi}\right)\right], \\ c_2 &\equiv -\frac{\partial}{\partial\xi}\left(\frac{1}{\sigma}\frac{\partial\sigma}{\partial\eta}\right), \quad c_3 \equiv \frac{2}{\mathscr{J}}\frac{\partial\mathscr{J}}{\partial\eta}, \quad c_4 \equiv -\frac{2}{\mathscr{J}}\frac{\partial\mathscr{J}}{\partial\xi}, \\ d_1 &\equiv -\left[\frac{1}{\mathscr{J}}\left(\frac{\partial^2\mathscr{J}}{\partial\xi^2} + \frac{\partial^2\mathscr{J}}{\partial\eta^2}\right) + \frac{2}{\sigma}\frac{\partial^2\sigma}{\partial\eta^2} + \frac{1}{\mathscr{J}\sigma}\left(\frac{\partial\sigma}{\partial\xi}\frac{\partial\mathscr{J}}{\partial\xi} - \frac{\partial\sigma}{\partial\eta}\frac{\partial\mathscr{J}}{\partial\eta}\right)\right], \\ d_2 &\equiv -\frac{\partial}{\partial\xi}\left(\frac{1}{\sigma}\frac{\partial\sigma}{\partial\eta}\right) \equiv d_3 \equiv -\frac{2}{\mathscr{J}}\frac{\partial\mathscr{J}}{\partial\eta} \equiv d_4 \equiv \frac{2}{\mathscr{J}}\frac{\partial\mathscr{J}}{\partial\xi}. \end{aligned} \tag{13}$$

The no-slip, no-penetration, and axial symmetry conditions require $u_\xi = 0$ at $\eta = 0$ and $|\xi| \leqslant \xi_s$, $\frac{\partial u_\xi}{\partial\eta} = 0$ at $\eta = 0$ and $|\xi| \geqslant \xi_s$, and $u_\eta = 0$, at $\eta = 0$. At the far-field, $\eta = \eta_t$, the free-slip condition is enforced, $u_\eta = 0$, and $\partial u_\xi/\partial\eta = 0$. To ensure that the effect of domain truncation is negligible, η_t is chosen to be eight times the thread radius. The corresponding outer radius of the axisymmetric computational domain is slightly larger than η_t. The specific value is determined by the mapping function, which is defined by the particle size and fundamental wave length. The grid is stretched in both the x and σ directions to accommodate the fine features of the flow, as shown in Fig. 3.

The traction jump due to the surface tension across the thread interface is implemented using Peskin's [11] immersed-interface method. In this approach, the location of the interface in a

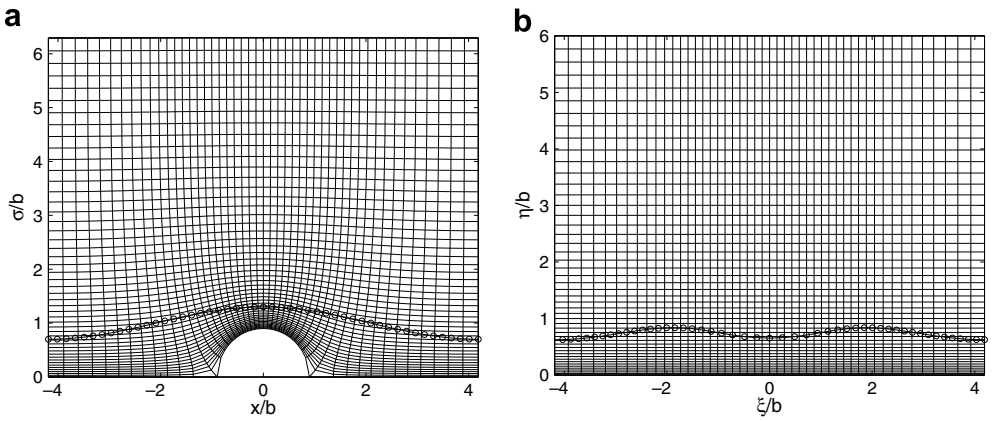

Fig. 3. (a) An orthogonal boundary-fitted curvilinear grid produced by conformal mapping, and (b) the mapped domain of flow. The distribution of the interfacial nodes is shown in both cases.

meridional plane is traced by a set of interfacial nodes, and the interfacial profile is reconstructed from nodal positions using periodic cubic-spline interpolation with respect to the polygonal arc length connecting adjacent nodes. The normal and tangential vectors and interfacial curvature are computed from the reconstructed representation. The discontinuous viscosity field is replaced with a smooth distribution, $\mu(\xi,\eta) = \mu_1 + (\mu_2 - \mu_1)c(\xi,\eta)$, where c is a mollifying (color) function taking the value of zero in the bulk of the thread fluid, the value of unity in the bulk of the ambient fluid, and undergoing a rapid transition across the interface. The gradient of the mollifying function, ∇c, points normal to the interface. Using an approximate delta function in place of $\mathscr{D}_2$ in (10), the singular traction jump across the interface due to the surface tension is regularized and incorporated as a narrowly distributed body force. Details are given elsewhere (e.g. [12,13,19]).

To compute the evolution of the flow from a specified initial condition, a variation of Chorin's projection method is employed. The algorithm involves a series of elementary sub-steps based on the constituent evolution equations

$$\begin{aligned}
&\rho\frac{\partial\hat{\mathbf{u}}}{\partial t} = \hat{\nabla}\mu\times\hat{\boldsymbol{\omega}} + \hat{\mathbf{B}} - \rho\hat{\mathbf{v}}\cdot\begin{bmatrix} \frac{u_\eta}{\mathscr{J}^2}\frac{\partial\mathscr{J}}{\partial\eta} & -\frac{u_\eta}{\mathscr{J}^2}\frac{\partial\mathscr{J}}{\partial\xi} \\ -\frac{u_\xi}{\mathscr{J}^2}\frac{\partial\mathscr{J}}{\partial\eta} & \frac{u_\xi}{\mathscr{J}^2}\frac{\partial\mathscr{J}}{\partial\xi}\end{bmatrix},\\
&\rho\left(\frac{\partial\hat{\mathbf{u}}}{\partial t} + \hat{\mathbf{v}}\cdot\hat{\nabla}^{(1)}\hat{\mathbf{u}}\right) = \mu\hat{\nabla}^2\hat{\mathbf{u}}, \quad \rho\frac{\partial\hat{\mathbf{u}}}{\partial t} = -\hat{\nabla}\phi,
\end{aligned} \tag{14}$$

where ϕ is a projection function regarded as an approximation of the pressure (e.g. [20]), and

$$\hat{\nabla}^{(1)}\hat{\mathbf{u}} \equiv \begin{bmatrix} \frac{1}{\mathscr{J}}\frac{\partial u_\xi}{\partial\xi} & \frac{1}{\mathscr{J}}\frac{\partial u_\xi}{\partial\eta} \\ \frac{1}{\mathscr{J}}\frac{\partial u_\eta}{\partial\xi} & \frac{1}{\mathscr{J}}\frac{\partial u_\eta}{\partial\eta}\end{bmatrix}. \tag{15}$$

To expedite the simulations, the second step in (14) is further decomposed into two one-dimensional convection–diffusion steps:

$$\begin{aligned}
&\rho\left(\frac{\partial\hat{\mathbf{u}}}{\partial t} + v_\xi\frac{1}{\mathscr{J}}\frac{\partial\hat{\mathbf{u}}}{\partial\xi}\right) = \mu\mathscr{L}^{(1)}(\hat{\mathbf{u}}),\\
&\rho\left(\frac{\partial\hat{\mathbf{u}}}{\partial t} + v_\eta\frac{1}{\mathscr{J}}\frac{\partial\hat{\mathbf{u}}}{\partial\eta}\right) = \mu\mathscr{L}^{(2)}(\hat{\mathbf{u}}) + \mu\mathscr{L}^{(3)}(\hat{\mathbf{u}}),
\end{aligned} \tag{16}$$

where $\mathscr{L}^{(i)}(\hat{\mathbf{u}})$, $i = 1, 2, 3$, are individual splittings of $\hat{\nabla}^2\hat{\mathbf{u}}$, given by

$$\mathscr{L}^{(1)}(\hat{\mathbf{u}}) \equiv \frac{1}{\mathscr{J}^2}\begin{bmatrix} \frac{\partial}{\partial\xi}\left(\frac{1}{\sigma}\frac{\partial\sigma u_\xi}{\partial\xi}\right) + c_1 u_\xi \\ \frac{1}{\sigma}\frac{\partial}{\partial\xi}\left(\sigma\frac{\partial u_\eta}{\partial\xi}\right) + d_1 u_\eta\end{bmatrix}, \tag{17}$$

$$\mathscr{L}^{(2)}(\hat{\mathbf{u}}) \equiv \frac{1}{\mathscr{J}^2}\begin{bmatrix} \frac{1}{\sigma}\frac{\partial}{\partial\eta}\left(\sigma\frac{\partial u_\xi}{\partial\eta}\right) \\ \frac{\partial}{\partial\eta}\left(\frac{1}{\sigma}\frac{\partial\sigma u_\eta}{\partial\eta}\right)\end{bmatrix}, \tag{18}$$

and

$$\mathscr{L}^{(3)}(\hat{\mathbf{u}}) \equiv \frac{1}{\mathscr{J}^2}\begin{bmatrix} c_2 u_\eta + c_3\frac{u_\eta}{\partial\xi} + c_4\frac{u_\eta}{\partial\eta} \\ d_2 u_\xi + d_3\frac{u_\xi}{\partial\xi} + d_4\frac{u_\xi}{\partial\eta}\end{bmatrix}. \tag{19}$$

The first equation in (14) is integrated forward in time using the explicit Euler method, while Eq. (16) are integrated using the implicit Crank–Nicolson method. The implicit treatment of $\mathscr{L}^{(3)}(\hat{\mathbf{u}})$ in the second sub-step of (16) requires the iterative updating of the velocity. Demanding that the third equation in (14) delivers a solenoidal velocity field at the end of a complete time step yields a Poisson equation for the projection function, $\hat{\nabla}^2\phi = (\rho/\Delta t)\hat{\nabla}\cdot\hat{\mathbf{u}}^*$, where Δt is the time step and $\hat{\mathbf{u}}^*$ is the intermediate velocity at the end of the convection–diffusion step. The solution is found by Gauss–Seidel iterations, subject to the periodic condition in ξ and the homogeneous Neumann boundary conditions at $\eta = 0$ and $\eta = \eta_t$.

Once the velocity field has been updated over a time step, the interfacial marker points are advanced in the physical space with the interpolated velocity field using the explicit Euler method. To obtain the interpolated values of the velocity field at the interfacial nodes, the Cartesian velocity field is calculated, the grid nodes are mapped to the $\xi\eta$ plane according to the mapping function (7), and the interpolation of the nodal velocity is carried out using the bicubic B-spline approximation in the $\xi\eta$ plane. The convection–diffusion Eq. (3) is simultaneously integrated using a finite-volume method [15].

4. Results and discussion

Blyth and Pozrikidis [10] confirmed that, in Stokes flow, the particle laden thread is unstable when the fundamental wave number, $kb = 2\pi b/L$, is less than the Plateau–Rayleigh threshold of unity. Because of the absence of a base flow, this threshold also holds in the presence of fluid inertia.

Simulations at low Reynolds numbers, $Re = \rho\gamma_0 b/\mu_1^2$, were successfully compared with predictions of the linear analysis for Stokes flow. At the initial instant, the cylindrical interface is displaced by a sinusoidal wave, $\sigma = b(1 + 0.05\cos(kx))$, while the fluids remain quiescent. In the first case study, the interface is devoid of surfactants; in the second case study, the surfactant concentration is initially uniform over the interface. Simulations were performed for $Re = 0.01$, $a/b = 0.2$, $D_s = 0$, and $\lambda = 0.5$, with time step $\Delta t = 0.001\,\mu_1 b/\gamma_0$ for the clean interface, and $\Delta t = 0.0002\mu_1 b/\gamma_0$ for the contaminated interface. An exceedingly small time step is necessary to ensure the longevity of the simulations at small Reynolds numbers. For $Ma = 0$ and $kb = 0.4\pi$, linear stability analysis for Stokes flow predicts the scaled growth rate $\hat{s} \equiv s\mu_1 b/\gamma_0 = -0.063$, and the numerical calculation yields $\hat{s} = -0.060$, where s is the dimensional growth rate. For $Ma = 0$ and $kb = 0.4$, linear analysis predicts $\hat{s} = 0.0469$, and the numerical calculation yields $\hat{s} = 0.0460$. For a contaminated interface with $Ma = 1$ and $kb = 0.4$, linear analysis predicts $\hat{s} = 0.0321$, and the numerical calculation yields $\hat{s} = 0.0395$. In all cases, the numerical simulations are in excellent agreement with the predictions of the linear analysis. The thread volume is reduced by less than 0.6% for the duration of a simulation, $\tau = t\,\gamma_0/(\mu_1 b) < 1$, due to numerical error. In extended simulations, the location of the interface is adjusted to offset this loss.

In the main simulations, the interface is initially displaced to the radial position $\sigma = b(1 \pm 0.3\cos kx)$. Consistent with linear analysis for Stokes flow at large and moderate wave numbers, the particle spacing is chosen to be the wavelength of the perturbation. The plus sign introduces a "peaked configuration" where the initial perturbation bulges over the particles, and the minus sign introduces a "depressed configuration" where the initial condition reaches a trough over the particles. A typical grid involves 48–108 divisions in the x-direction depending on the particle spacing, and 64 divisions in the σ direction. Each simulation takes approximately 6–10 h of CPU time on a single Xeon X5355 2.66 GHz processor.

Fig. 4a–d illustrates the evolution of one period of the interfacial profile for $a/b = 0.5$, $kb = 0.75$, $\lambda = 0.5$, and several Reynolds numbers, $Re = 0.01$, 20, 100, and 200. In all cases, the interfacial deflection amplifies due to the capillary instability, and the thread eventually breaks up into an array of droplets connected by ligaments,; each droplet encloses one particle. Secondary ligament breakup due to the capillary instability occurs at the late stages of the instability producing small satellite drops. For $Re = 20$, 100, and 200, the thread is the thinnest near the tips of the encapsulating drops.

Although the details of the evolution are similar in all cases described in Fig. 4a–d, significant differences regarding the growth rate of the instability arise. Fig. 4e shows a graph of the interfacial amplitude, A, reduced by the initial amplitude, A_0, plotted against

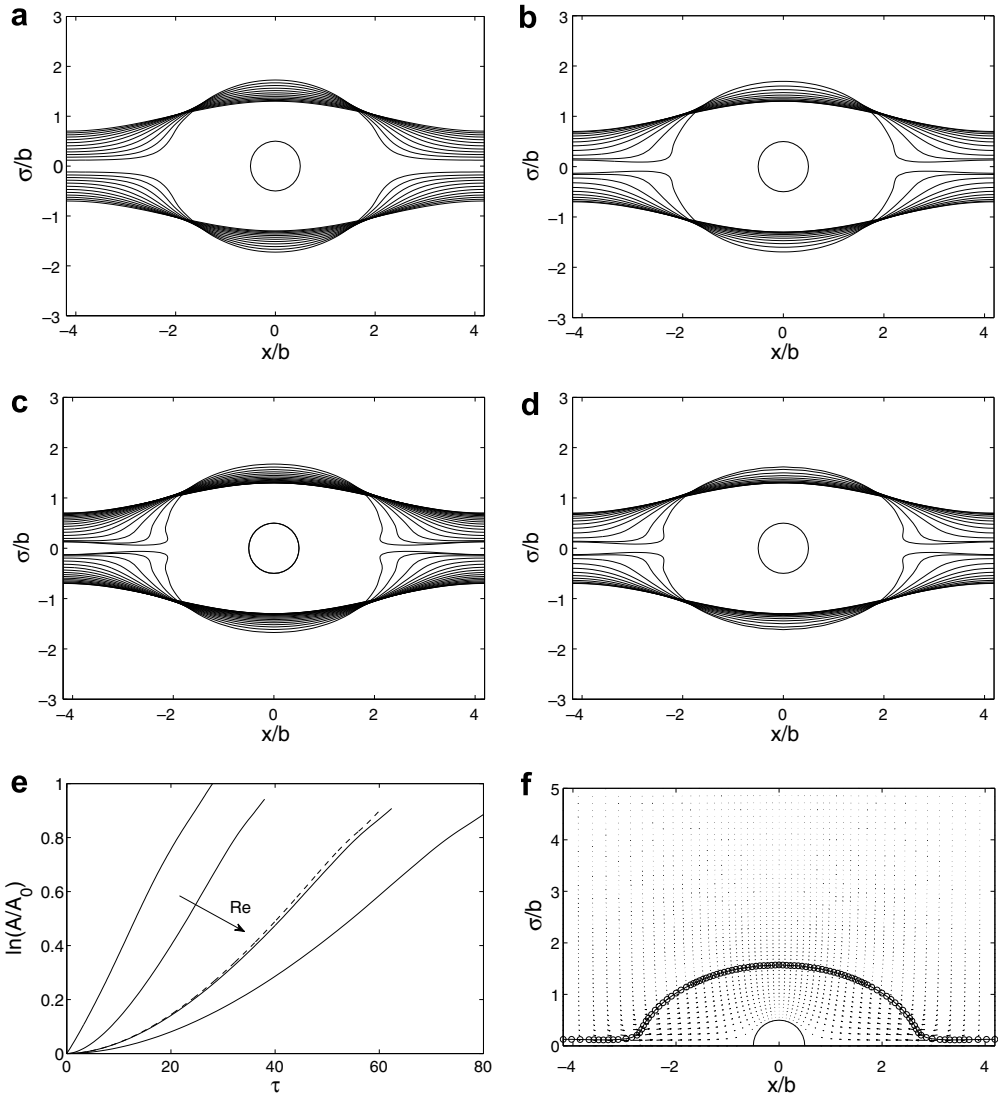

Fig. 4. (a–d) Evolution of the interfacial instability for $a/b = 0.5$, $kb = 0.75$, $\lambda = 0.5$, and (a) $Re = 0.01$, (b) $Re = 20$, (c) $Re = 100$, and (d) $Re = 200$, in the absence of surfactants. (e) Growth rate plotted against normalized time, $\tau = t\gamma_0/(\mu_1 b)$, where A_0 and A are the initial and current amplitudes. A grid resolution of 48×64 is used in these simulations. The dashed line corresponds to a simulation for $Re = 100$ with doubled grid resolution. (f) Velocity vector field and interfacial profile at the final stage of simulation for $Re = 200$.

the dimensionless time, $\tau = t\gamma_0/(\mu_1 b)$. A simulation for $Re = 100$ with doubled grid resolution is shown to confirm the accuracy of the results obtained by the standard resolution. In the case of low-Reynolds-number flow, the growth rate remains nearly constant over an extended period of time. At higher Reynolds numbers, the interfacial growth is initially slow as the fluid gains momentum. After an initial start-up period whose duration increases as the Reynolds number is raised, the growth curves exhibit well-defined slopes equal to 0.03 for $Re = 20$, 0.018 for $Re = 100$, and 0.015 for $Re = 200$. The linear growth rates represented by these slopes significantly decrease as the Reynolds number becomes higher.

A linear stability analysis for a pure thread conducted using codes provided in the software library FDLIB [21] predicts normal mode growth rates 0.0278 for $Re = 20$, 0.0181 for $Re = 100$, and 0.0143 for $Re = 200$, which are very close to the values extracted from the numerical simulations. We conclude that the particles have a small effect on the onset of the instability. At the final stage of the evolution, the growth of the interfacial amplitude slows down, and the developed drops begin contracting along the thread axis. Fig. 4f shows the interfacial profile and velocity vector field for $Re = 100$ at the end of the simulation. Close inspection demonstrates the pronounced stretching of the interface between pairs of developing drops.

A second set of simulations is shown in Fig. 5a and c to demonstrate the effect of the wave number for $a/b = 0.5$, $\lambda = 0.5$, fundamental wave number $kb = 0.4$, and $Re = 0.01$ and 100. The general features of the instability are similar to those shown in Fig. 3 for the larger wave number. One significant difference is that two arrays of drops connected by cylindrical bridges develop at the low Reynolds number. In this case, the thread is expected to break up into a sequence of pure drops, another sequence of encapsulating drops, and an array of small satellite drops originating from the bridges. For $Re = 0.01$, the pure and encapsulating drops develop at similar speeds, whereas for $Re = 100$, the pure drops develop much slower than the encapsulating drops. The volume of the drops encapsulating the particles is significantly larger than that of the pure drops.

Fig. 5b and d illustrates the evolution of the thread for $Re = 0.01$, 100, and a larger particle, $a/b = 0.9$. Comparing these profiles to those presented in Fig. 5a and c, we find that the particle size significantly affects the development of the instability at the low Rey-

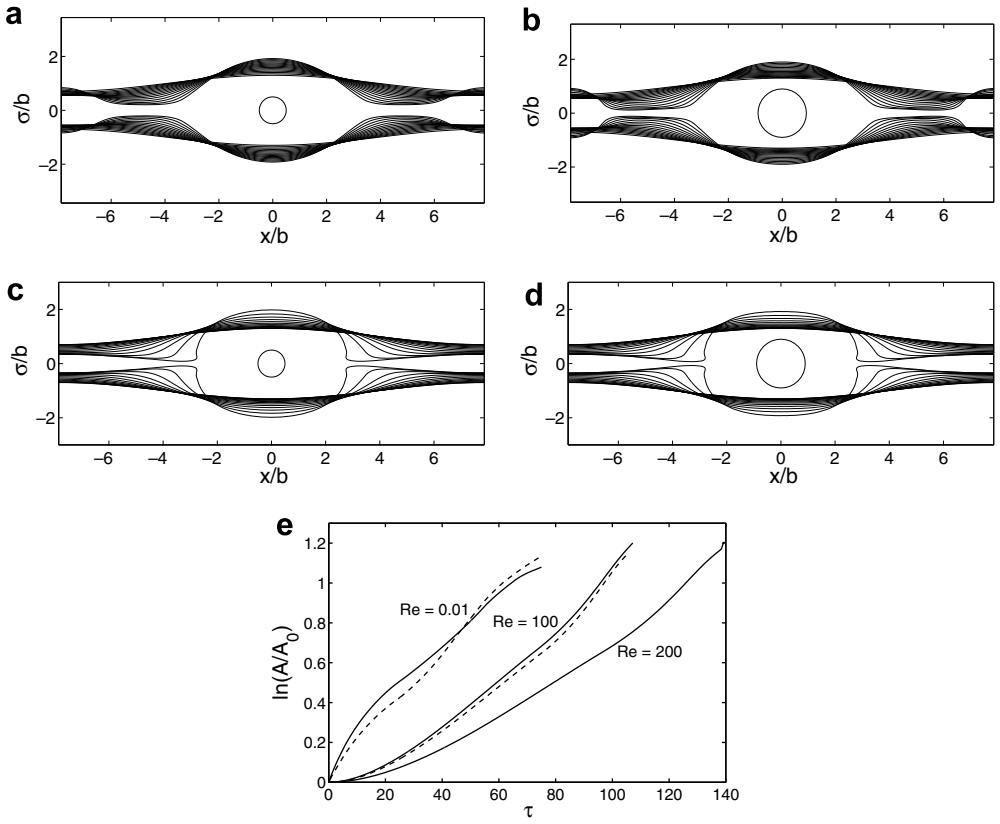

Fig. 5. (a–d) Evolution of the clean interface for $kb = 0.4$, $\lambda = 0.5$ and (a) $Re = 0.01$, $a/b = 0.5$, (b) $Re = 0.01$, $a/b = 0.9$, (c) $Re = 100$, $a/b = 0.5$, (d) $Re = 100$, $a/b = 0.9$. (e) Growth of the wave amplitude plotted against normalized time, $\tau = t\gamma_0/(\mu_1 b)$. for $Re = 0.01$, 100, 200. Corresponding cases for $a/b = 0.9$ and $Re = 0.01$, 100 are shown as dashed lines.

nolds number, $Re = 0.01$. At the late stages of the instability, the pure drops develop faster for $a/b = 0.9$ than $a/b = 0.5$. However, the effect is hardly noticeable at the high Reynolds number, $Re = 100$. The influence of the particle size is better demonstrated in Fig. 5e illustrating the growth of the interfacial amplitude. Once again, we observe that fluid inertia delays the growth of interfacial undulations. Comparing the curves at $Re = 100$ for particle size, $a/b = 0.5$ and 0.9, we find that the growth of the perturbation is only slightly lower for the large particles. The significant effect of the particle size for $Re = 0.01$ is consistent with the linear stability analysis of Blyth and Pozrikidis [10] for unit viscosity ratio.

A further set of simulations was carried out for $a/b = 0.5$, $Re = 100$, $kb = 0.75$ or 0.4 to study the effect of the viscosity ratio. Fig. 6a and b shows the growth of the surface amplitude for $\lambda = 0.5$, 1 and 5. For both wave numbers, the growth rate of the instability decreases significantly as the viscosity ratio is raised and the ambient fluid becomes more viscous. The interfacial evolution for $\lambda = 5$ is illustrated in Fig. 6c and d. At $kb = 0.75$, the linear growth rate after the initial transient stage is 0.018, 0.016, 0.01 for $\lambda = 0.5$, 1, 5. Linear stability analysis of the pure thread at this Reynolds number predicts the virtually identical growth rates 0.0181, 0.0162, and 0.0106. At $kb = 0.4$, the linear growth rate after the initial transient stage is 0.012, 0.01, 0.0066 for $\lambda = 0.5$, 1, 5. Linear stability analysis of the pure thread predicts the somewhat higher growth rates 0.0154, 0.0137, and 0.0094. Comparing corresponding results for $\lambda = 0.5$ in Figs. 4c and 5c, we find that the viscosity ratio does not radically affect the interfacial morphology developing from the instability.

The linear analysis for Stokes flow undertaken in [10] has indicated that, as the wave number is reduced, the superharmonic components of the normal modes become increasingly important. To investigate the significance of particle spacing in the presence of fluid inertia, simulations were performed for $a/b = 0.5$, $\lambda = 0.5$, $Ma = 0$, and $kb = 0.3$. The initial interfacial perturbation is either the fundamental wave $0.3b\cos(kx)$, or its first harmonic wave, $0.3b\cos(2kx)$. The latter is an approximation of the most dangerous normal mode in Stokes flow. Fig. 7a and b shows the interfacial evolution for the two initial conditions at $Re = 100$. In the first case, one period of the thread breaks up at two locations, forming two sequences of drops. The pure drops are significantly smaller than the encapsulating drops. In the second case, one period of the thread breaks up at three locations, forming one sequence of encapsulating drops and two sequences of pure drops. One sequence of pure drops is comparable in size to the encapsulating drops, while the drop in the other sequence are much smaller. Comparing the growth rates of the instability, shown in Fig. 7c, we find that the harmonic wave grows much faster than the fundamental wave. Consequently, breakup at the harmonic scale is more likely to occur in practice. Fig. 7d shows the velocity vector field of the fluid inside each drop and ambient fluid, confirming the axial contraction of the drops.

Fig. 8a describes the growth of a contaminated interface for $Ma = 4$, $kb = 0.4$, $a/b = 0.5$, $Re = 100$, and $\lambda = 0.5$. Compared to a clean interface at the same wave number and viscosity ratio, the growth of the contaminated thread is significantly slower at the late stages of the evolution. The interface profile, surfactant concentration, and surface tension are shown in Fig. 8b. As in the case of a clean thread, the contaminated thread breaks up at two locations between two adjacent particles. Comparing the interfacial profiles at the late stage of the evolution with those of a clean thread, shown as dotted lines in Fig. 8b, we find that the surfactant expedites the growth of the developing pure drop relative to the main drop encapsulating the particle. The surfactant concentration is low at the throat of the thread due to stretching of the interface,

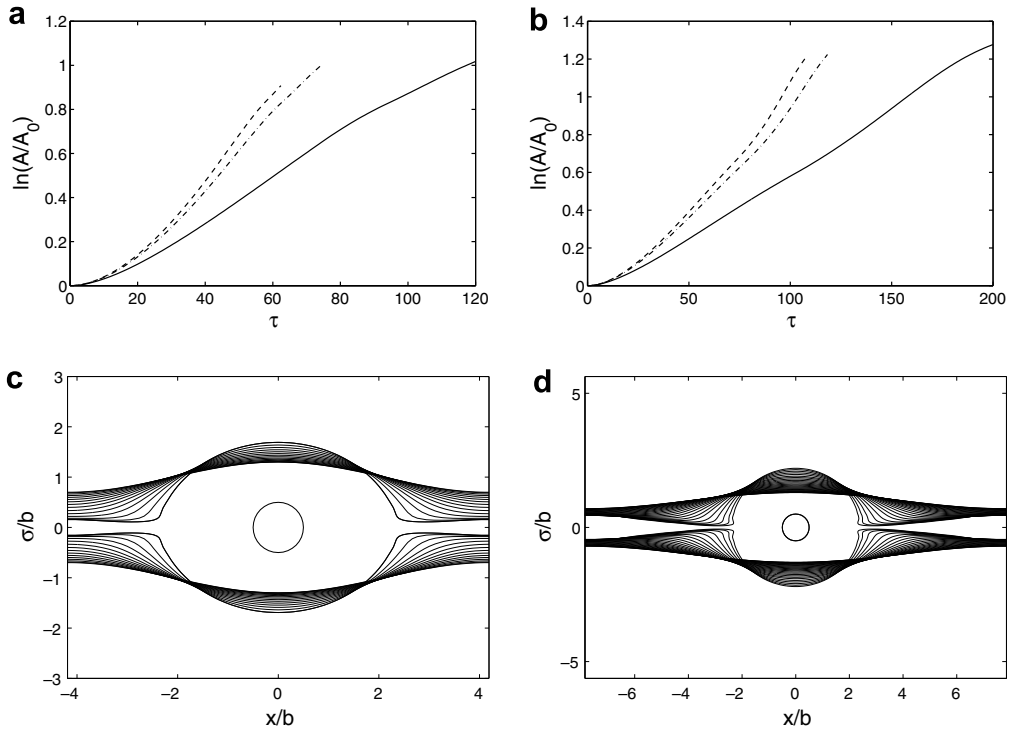

Fig. 6. (a–b) Growth of the interfacial amplitude for a clean interface plotted against normalized time, $\tau = t\gamma_0/(\mu_1 b)$, for $a/b = 0.5$, $Re = 100$, and $\lambda = 0.5$ (dashed lines), 1 (dash-dotted lines), and 5 (solid lines). The wave number is $kb = 0.75$ in (a) and 0.4 in (b). Corresponding interface evolutions are shown for $\lambda = 5$ and (c) $kb = 0.75$, (d) $kb = 0.4$.

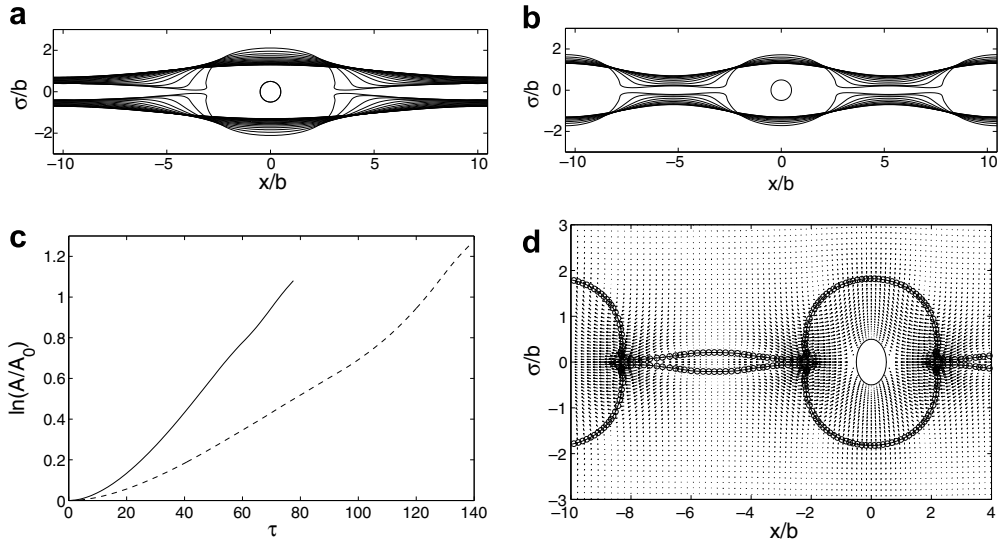

Fig. 7. (a) and (b) Evolution of the clean interface for $a/b = 0.5$, $kb = 0.3$, $\lambda = 0.5$ and $Re = 100$. The initial perturbation to the interface was set to $0.3b\cos(kx)$ in (a) and $0.3b\cos(2kx)$ in (b). (c) Corresponding growth of the interface for (a) (dashed line) and (b) (solid line). (d) Velocity field near breakup for (b).

and nearly uniform elsewhere. Correspondingly, the surface tension is high at the throat and low elsewhere. In summary, the surfactant has a significant effect on the development of pure liquid drops.

In the numerical simulations discussed thus far, we have considered perturbations that deflect the interface away from the particle surface at the initial instant. The effect of the depressed configuration on the interfacial evolution is demonstrated in Fig. 9 where the sinusoidal perturbation deflects the interface toward the particle surface at the initial instant $\sigma = b(1 - 0.3\cos(kx))$. The simulation parameters are $a/b = 0.5$, $Ma = 0$, $Re = 100$, $\lambda = 0.5$, and $kb = 0.75$ or 0.4. When $kb = 0.75$, the instability is nearly suppressed as the interface approaches the particle surface to form a sequence of particles connected by axisymmetric bridges. When $kb = 0.4$, the interfacial growth is also nearly suppressed over the particle, but the liquid bridges connecting the particles continue to develop. Breakup produces a sequence of smaller encapsulating drops, a sequence of larger pure drops, and satellite drops. A similar behavior for the depressed configuration was observed in boundary-integral simulations for Stokes flow by Blyth and Pozrikidis [10].

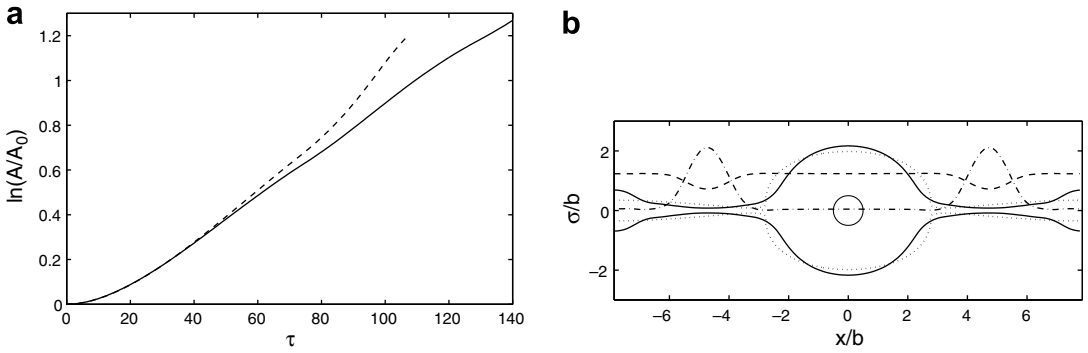

Fig. 8. (a) Growth of the wave amplitude for $kb = 0.4$, $a/b = 0.5$, $\lambda = 0.5$, $Re = 100$, and $Ma = 4$ (solid line) or $Ma = 0$ (dashed line). (b) Interface profile (solid line), surfactant concentration (dashed line), and surface tension distribution (dashed-dotted line) for $Ma = 4$. The interface for the clean thread at final stage is drawn as a dotted line.

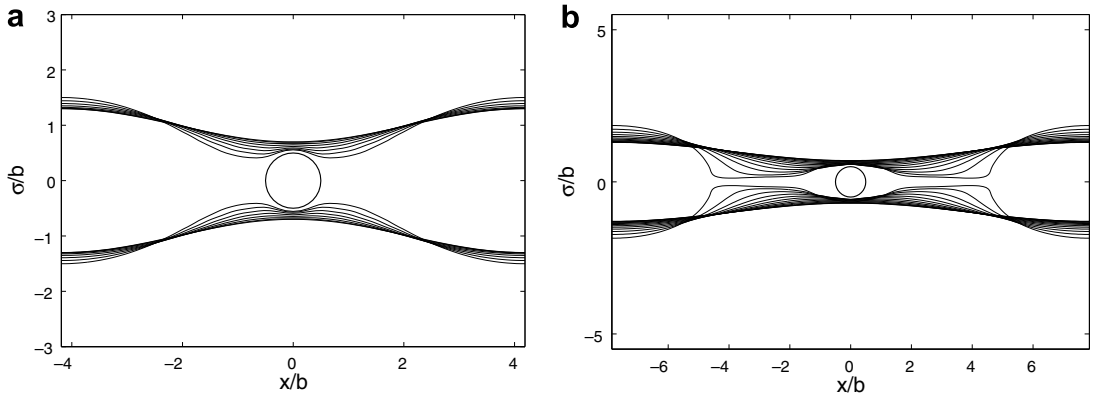

Fig. 9. Evolution of a clean interface in the depressed configuration for $a/b = 0.5$, $\lambda = 0.5$, $Re = 100$, and (a) $kb = 0.75$, (b) $kb = 0.4$.

5. Conclusion

We have carried out numerical simulations at finite Reynolds numbers to describe the nonlinear stages of the capillary instability of a particle laden liquid thread, and investigated the effect of the viscosity ratio, Reynolds number, particle size and spacing, Marangoni number, and initial perturbation type. The results complement the linear stability analysis and simulations of Blyth and Pozrikidis [10] for Stokes flow. We have found that the thread breaks up into droplets encapsulating particles and pure fluid. Inertia has a significant effect on the growth rate of the instability and nature of thread breakup. As the Reynolds number increases, the growth of the instability slows down and the effect of the particle size becomes less important. Increasing the viscosity of the ambient fluid or the Marangoni number reduces the rate of interfacial growth. The particle spacing and form of the initial perturbation may dramatically change the morphology of the thread breakup. Overall, our numerical results offer useful guidelines for the design of equipment in micro-encapsulation technology.

Acknowledgement

This research was supported by a grant from the National Science Foundation and the Vanderbilt University.

References

[1] Goosen MFA, O'Shea GM, Gharapetian HM, Chou S, Sun AM. Optimization of micro-encapsulation parameters: semipermeable micro-capsules as a bio-artificial pancreas. Biotechnol Bioeng 1985;27(2):146–50.
[2] Orive G, Hernandez RM, Gascon AR, Callafiore R, Chang TMS, Hortelano G et al. Cell encapsulation: promise and progress. Nat Med 2003;9:104–7.
[3] Tomotika S. On the instability of a cylindrical thread of a viscous liquid surrounded by another viscous fluid. Proc Roy Soc A 1935;150:322–37.
[4] Grotberg JB. Pulmonary flow and transport phenomena. Annu Rev Fluid Mech 1994;26:529–71.
[5] Papageorgiou DT. On the breakup of viscous liquid threads. Phys Fluids 1995;7:1529–44.
[6] Kwak S, Pozrikidis C. Effect of surfactants on the instability of a liquid thread or annular layer. Part I. Quiescent fluids. Int J Multiphase Flow 2001;27:1–37.
[7] Deng Q, Anilkumar AV, Wang TG. The role of viscosity and surface tension in bubble entrapment during drop impact onto a deep liquid pool. J Fluid Mech 2007;578:119–38.
[8] Shintaku H, Kuwabara T, Kawano S, Suzuki T, Kanno I, Kotera H. Micro cell encapsulation and its hydrogel-beads production using microfluidic device. Microsyst Technol 2007;13:951–8.
[9] Skurtys O, Aguilera JM. Applications of microfluidic devices in food engineering. Food Biophys 2008;3:1–15.
[10] Blyth MG, Pozrikidis C. Particle encapsulation due to thread breakup in Stokes flow, submitted for publication.
[11] Peskin CS. The immersed boundary method. Acta Numer 2002;11:479–517.
[12] Blyth MG, Luo H, Pozrikidis C. Stability of axisymmetric core-annular flow in the presence of an insoluble surfactant. J Fluid Mech 2006;548:207–35.
[13] Luo H, Blyth MG, Pozrikidis C. Two-layer flow in a corrugated channel. J Eng Math 2008;60:127–47.
[14] Li X, Pozrikidis C. Effect of surfactants on drop deformation and on the rheology of dilute emulsions in Stokes flow. J Fluid Mech 1997;341:165–94.
[15] Yon S, Pozrikidis C. A finite-volume/boundary-element method for interfacial flow in the presence of surfactants, with applications to shear flow past a viscous drop. Comput Fluids 1998;27:879–902.
[16] Adamson AW. Physical Chemistry of Surfaces. London: Wiley; 1990.
[17] Pozrikidis C. Instability of multi-layer channel and film flows. Adv Appl Mech 2004;40:179–239.
[18] Pozrikidis C. Boundary conditions for shear flow past a permeable interface modeled as an array of cylinders. Comput Fluids 2004;33:1–17.
[19] Pozrikidis C. Effect of inertia on the Marangoni instability of two-layer channel flow, Part I: numerical simulations. J Eng Math 2004;50:311–27.
[20] Pozrikidis C. Introduction to theoretical and computational fluid dynamics. New York: Oxford University Press; 1997.
[21] Pozrikidis C. Fluid dynamics: theory, computation and numerical simulation. Kluwer Academic Publishers; 2001.